Doppler Optical Coherence Tomography Signals: Analysis in Low and High Scattering Media

21

Alexander V. Bykov and Jeroen Kalkman

Contents

Abstract

In this chapter, Doppler OCT signals (OCT magnitude and flow velocity profile) for low and high scattering media are analyzed. For low scattering media, we demonstrate the use of the single scattering model to determine the optical properties of the sample. For high scattering media, the effects of multiple scattering are stronger and the single scattering description breaks down. An alternative approach, based

A.V. Bykov (✉)
Optoelectronics and Measurement Techniques Laboratory, University of Oulu, Oulu, Finland
e-mail: bykov@ee.oulu.fi

J. Kalkman
Biomedical Engineering & Physics, Academic Medical Center, University of Amsterdam, Amsterdam, The Netherlands
e-mail: j.kalkman@amc.uva.nl

V.V. Tuchin (ed.), *Handbook of Coherent-Domain Optical Methods*,
DOI 10.1007/978-1-4614-5176-1_21,

on Monte Carlo simulations, is proposed as it gives a more appropriate description of the Doppler OCT signal by taking into account multiple scattering effects. Using Monte Carlo simulations, we analyze the deviation of the OCT slope from the value predicted by the single scattering model and analyze the distortions in the measured Doppler OCT flow profile. Monte Carlo simulations are compared to Doppler OCT measurements for Intralipid and blood.

21.1 Introduction

Optical coherence tomography (OCT) is a relatively new biomedical imaging technique that is used in clinical diagnostics, treatment monitoring, and disease prevention (screening). OCT is based on low-coherence interferometry and provides micrometer resolution images of turbid media up to a few millimeters deep. Besides morphological images, OCT also can be used to determine functional tissue parameters such as the light attenuation coefficient [1], (blood) flow [2], and tissue birefringence [3]. Since its invention [4], OCT has been applied in ophthalmology, vascular imaging, dermatology, and many other areas.

In this chapter, we analyze the Doppler OCT signal in low and high scattering media. For low scattering media the Doppler OCT signal is well described by the single scattering model, which is discussed in Sect. 21.2 As described in Sect. 21.3 optical properties such as the scattering coefficient, the scattering cross section, and the scattering anisotropy can be extracted directly from the OCT signal using the single scattering model. The single scattering model also provides a good description of the Doppler OCT signal and is used to quantify flow. In Sect. 21.4 we show that for high scattering media, the single scattering approximation is no longer an appropriate model to describe the Doppler OCT signal. To describe the Doppler OCT signal for high scattering media, we use Monte Carlo simulations, as explained in Sect. 21.5 to simulate the Doppler OCT signal as shown in Sect. 21.6. We focus on Intralipid and blood as scattering media as they differ in their scattering coefficient and scattering anisotropy. Finally in Sect. 21.7 we compare the Monte Carlo simulations to the Doppler OCT measurements for Intralipid and blood. We observed good agreement between our simulations and the measurements.

21.2 Single Scattering Description of the Doppler OCT Signal

In its most basic form, OCT is based on single backscattering imaging. Light incident on the sample travels in a ballistic straight path through the scattering medium until a single backscatter event reflects the light back into the sample arm optics. Multiple scattered light is rejected by the combination of confocal detection and coherent gating. In confocal detection, axial and lateral out of focus light is rejected due to the lower back-coupling efficiency. Moreover, out of focus light has traveled a longer path length and therefore is mapped onto larger depths in the sample, thereby reducing its effect on the shallower OCT signals. For low scattering

media multiple scattered light is efficiently rejected from the OCT signal and the single scattering approximation is a valid description for the OCT signal.

For the single scattering approximation of the OCT signal, we assume a loss less time-domain OCT system without focus tracking. The OCT detector current $i_{det}(z)$ as a function of depth z, is equal to the backscatter profile of the sample as a function of z convoluted with the complex coherence function γ $(2z/c)$ [5]. For a single perfect mirror in air positioned in the sample arm located at $z = 0$, the OCT detector current signal is

$$i_{\mathrm{det}}(z) = \eta \mathrm{Re}\left\{\gamma\left(\frac{2z}{c}\right)\right\} \otimes r_{mirror} h(z)\delta(z)\sqrt{P_{ref}P_{sample}}, \tag{21.1}$$

where η is the detector conversion factor from the incident light power to the electric current, Re{} is the real part of the complex coherence function, c is the speed of light, r_{mirror} is the field reflection coefficient of the mirror, $h(z)$ is the confocal point spread function [6], $\delta(z) = 1$ for $z = 0$ and $\delta(z) = 0$ for all other z. The powers P_{ref} and P_{sample} are the powers incident on the reference and sample arm, respectively. Performing the convolution in (21.1) and taking the square of the OCT signal at $z = 0$, we find

$$i_{\mathrm{det}}(z=0)^2\big|_{mirror} = \eta^2\, r_{mirror}^2 P_{ref} P_{sample}, \tag{21.2}$$

where it is assumed that $h(0) = 1$, i.e., the mirror is in the focus of the sample arm focusing lens. For a scattering medium without absorption, the situation is more complicated. A one-dimensional single scattering model is assumed where homogenously distributed scatterers all add coherently to the OCT signal. Assuming that the OCT signal for a homogenous scattering medium is the sum of all scattering contributions, the detector current is

$$i_{\mathrm{det}}(z) = \eta \mathrm{Re}\left\{\gamma\left(\frac{2zn_{med}}{c}\right)\right\} \otimes h(z)\sqrt{P_{ref}P_{sample}}\sqrt{\mu_{b,NA}}\sqrt{\exp(-2\mu_s z)}, \tag{21.3}$$

with n_{med} the group refractive index of the medium, $\mu_{b,NA}$ the effective backscattering coefficient (quantifying the part of the light that is backscattered into the detection numerical aperture (NA) of the OCT system). The scattering coefficient μ_s is equal to the concentration of scatterers C and their cross section σ_s, i.e., $\mu_s = C\sigma_s$. The factor 2 in the exponent of (21.3) accounts for the round-trip attenuation to and from depth z. In a scattering medium with attenuation μ_s, the amplitude of the OCT signal can be found by extrapolating the attenuated OCT signal to $z = 0$. The square of the OCT signal at the interface is

$$i_{\mathrm{det}}(z=0)^2\big|_{scat} = \eta^2 \frac{l_c}{n_{med}} P_{ref} P_{sample} \mu_{b,NA}\, Q, \tag{21.4}$$

where the coherence length l_c is defined in single pass according to Schmitt et al. [7] and Goodman [5]. Note that this coherence length definition is a factor $(\pi/8\ln 2)^{1/2} \approx 0.75$ smaller than the commonly used definition related to the axial resolution in OCT that is defined as the full width at half maximum of the Gaussian–shaped coherence point spread function of the OCT amplitude [8].

The constant Q describes the heterodyne intensity back-coupling efficiency from a scattering medium compared to that of a mirror and ranges from 0 to 1. There are two main reasons that cause a reduction of the heterodyne detection efficiency Q for a homogenous distribution of scatterers compared to a mirror to values less than 1. First, the OCT magnitude for a sum of scatterers depends on the random axial position of the scatterers in the sample (causing speckle). As a result, the envelope of the OCT signal (e.g., the mean value of the speckle pattern) is smaller than the addition of all individual particle envelopes. Second, the OCT backscatter efficiency for small particles depends on the lateral offset of the scatterer in the focused beam. For particles not on the optical axis, the spherical wave originating from a particle is less efficiently coupled back to the single mode fiber compared to the planar wavefront reflected from the mirror.

From this analysis, it can be observed that μ_b can be determined by dividing (21.2) by (21.4). The backscattering coefficient is

$$\mu_{b,NA} = \frac{i_{\mathrm{det}}(z=0)^2\big|_{scat}}{i_{\mathrm{det}}(z=0)^2\big|_{mirror}} \frac{n_{med} r_{mirror}^2}{l_c Q} = p_{NA}\mu_s, \tag{21.5}$$

with the backscattering coefficient μ_b equal to the scattering coefficient times the phase function integrated over the NA in the backscattering direction, p_{NA}. Note that by taking the ratio of two OCT measurements additional loss factors in the OCT system do not influence the determination of μ_b. In the absence of absorption, the scattering coefficient μ_s can be determined from the slope of the OCT signal. For media with absorption and described by the single scattering approximation, light travels in a ballistic way and Beer's law can be applied to calculate the total OCT attenuation coefficient μ_t, which equals $\mu_t = \mu_s + \mu_a$. Consequently, μ_s can be obtained by subtracting the absorption coefficient from the total attenuation coefficient obtained from the slope of the OCT signal. The scattering phase function in the backscattering direction can be obtained by integrating the scattering phase function $p(\theta)$ over angles from π-NA to π. The phase function integrated over the NA, p_{NA}, describes the fraction of scattered photons that are detected by the OCT system, i.e., $p_{NA} = \mu_{b,NA}/\mu_s$. Consequently, p_{NA} can be determined using (21.5) and μ_s

$$p_{NA} \equiv \int_{\pi-NA}^{\pi} p(\theta) 2\pi \sin(\theta) d\theta = \frac{\mu_{b,NA}}{\mu_s} = \frac{n_{med} r_{mirror}^2}{l_c Q \mu_s} \frac{i_{\mathrm{det}}(z=0)^2\big|_{scat}}{i_{\mathrm{det}}(z=0)^2\big|_{mirror}}. \tag{21.6}$$

Since p_{NA} is related to the phase function, the scattering anisotropy g can be determined from a determination of p_{NA} if the NA and the shape of the phase function is known a priori.

In the single scattering approximation, light is backscattered once and the Doppler frequency shift $f_{Doppler}$ of the backscattered light is determined by the incident angle θ, refractive index of the medium n, wavelength λ, and the flow speed v according to

$$f_{Doppler} = \frac{2vn}{\lambda} \cos\theta. \tag{21.7}$$

Note that for forward scattering the Doppler frequency shift is zero.

21.3 Determination of Optical Properties and Flow from Doppler OCT Signals of Low Scattering Media

The optical parameters of low scattering media are determined using a home-built time-domain OCT system, which is described in detail in Ref. [9]. The time-domain OCT system is based on a filtered Fianium light source with the center wavelength at 1,300 nm. The axial resolution of this system is 9.7 ± 0.1 μm as was determined from the full width at half maximum of the OCT magnitude point spread function. The Gaussian beam waist of the focusing lens is 9.6 ± 0.2 μm, corresponding to a numerical aperture $NA = 0.043 \pm 0.001$. Prior to the experiment, the OCT system is calibrated for quantitative measurements of the backscattered power. Due to the limited dynamic range of the OCT system, the power from the mirror is measured using different calibrated neutral density filters in the sample arm. From the dependence of the OCT signal on the optical attenuation the reflected power and the OCT magnitude can be directly compared to the signals for the scattering sample in (21.6) (i.e., with no optical attenuation in the sample arm).

OCT measurements on suspensions of scatterers are performed in a 1 mm thick glass cuvette, placed in the sample arm at ~70° angle relative to the incident beam. The sample arm beam is focused at the first glass-medium interface. Measurements for every solution are performed independently for five times, averaging 100 A-scans per measurement. After background subtraction the OCT signal magnitude is corrected for the confocal point spread function [6], the optical path length is converted to depth using the refractive index of water [10]. The OCT attenuation coefficient is determined with a two parameter single exponential fit of the measured OCT signal in depth. To reduce the effects of multiple scattering, the concentration of scatterers is kept low to create samples with scattering coefficients below 5 mm^{-1} (as calculated with Mie theory). In addition, only OCT signals starting at ~60 μm depth after the sample front surface and extending 190 μm in depth is used for fitting the single exponential decay. The scattering coefficient μ_s is calculated by subtracting the water absorption coefficient ($\mu_a = 0.2\ mm^{-1}$) from the fitted attenuation coefficient μ_t. Finally, the scattering cross section σ_s is calculated

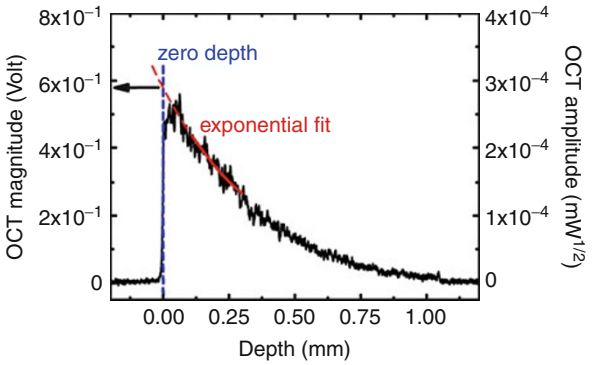

Fig. 21.1 OCT measurement of backscattered power from a suspension of 400 nm diameter polystyrene microspheres in water. The vertical scale on the *left* is converted to absolute units of square root of power using the power calibration and is indicated on the *right*. The attenuation coefficient is determined from the single exponential decay fit (*solid red line*); the amplitude of the OCT signal from the sample surface is determined by extending the exponential (*dashed red line*) fit to intersect with a drop line at zero depth (*dashed blue line*)

by dividing the scattering coefficient by the known particle concentration. The OCT signal amplitude at the front glass-sample interface is determined from the exponential fit by extending the fitting line to zero depth, as is shown in Fig. 21.1. The zero depth location is determined from the crossing of the OCT signal with the vertical drop line at half height of the OCT signal. Using our calibration method, the OCT signal magnitude is determined on an absolute scale in $mW^{1/2}$ units, which is indicated in Fig. 21.1 on the right hand side scale for a measurement of a scattering medium for 400 nm diameter particles. The peak of the backscattered power in the heterodyne (OCT) signal is of the order of 90 pW.

Polystyrene microspheres (Thermo Scientific, USA) are used as scatterers with the concentration of the sample calculated based on the used dilution (1 wt% concentration). The microspheres have mean diameters of 203 ± 5, 400 ± 9, 596 ± 6, 799 ± 9, and 994 ± 10 nm and size distribution standard deviations of 4.7, 7.3, 7.7, 4.8, and 10 nm, respectively. Mie calculations are performed based on mean diameters to calculate the scattering cross section and phase function of the polystyrene particles. The refractive index of water ($n_{water} = 1.32$ [10]) and polystyrene are used ($n_{polyst} = 1.57$ [11]) as input. From Mie calculations, the scattering anisotropy, i.e., the g of these microspheres, is calculated to be: 0.07, 0.29, 0.62, 0.73, and 0.81 for increasing sphere diameter. Also, from the calculated phase functions, the scattering efficiency in the backscattering direction p_{NA} is calculated by integrating the phase function over the *NA* of the sample arm focusing lens.

Measurements performed on Intralipid samples are used as an example of our technique to a polydisperse medium. Intralipid is an aqueous suspension of polydisperse lipid droplets, which is often used as a tissue phantom for optical measurements. To reduce any effects of multiple scattering, we performed measurements for low concentrations Intralipid (0.63, 1.25, and 2.5 wt%).

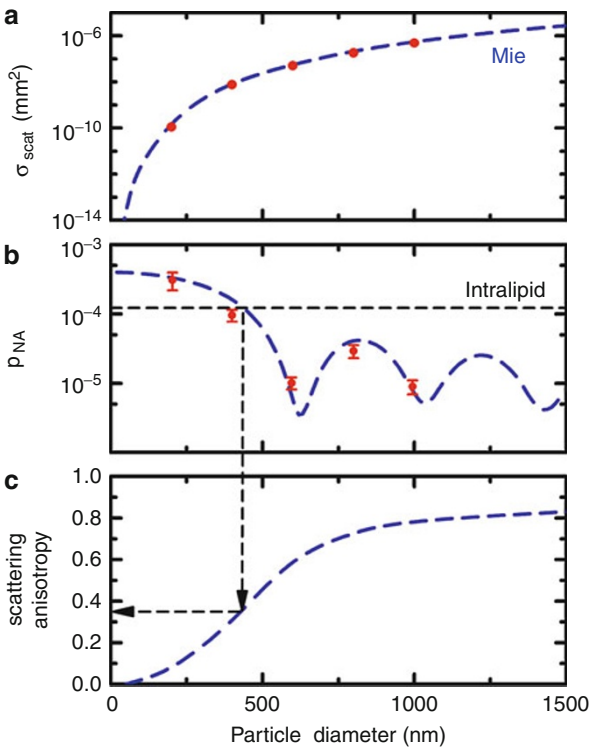

Fig. 21.2 Results of Mie calculations and experimental measurements of: (**a**) scattering cross section of polystyrene microspheres (error bars are smaller than symbols); (**b**) scattering phase function p_{NA} of polystyrene microspheres (error bars are standard deviations); the *dashed line* indicates the measured value of p_{NA} for Intralipid (standard deviation is given in the text); (**c**) Mie calculations of g versus particle diameter at 1,300 nm for polystyrene microspheres. *Arrows* show the average particle diameter and the g of Intralipid

The samples are prepared by dilution of a single batch of 20 wt% Intralipid (Fresenius-Kabi) with deionized water. The refractive indices used for Mie calculations of Intralipid are: $n_{water} = 1.32$ [10] for water; $n_{lip} = 1.46$ for lipid droplets [12].

From an OCT measurement as shown in Fig. 21.1, the scattering coefficient for a solution of particles is determined. Figure 21.2a shows the scattering cross section of polystyrene microspheres for the different diameters obtained from the scattering coefficient. The experimental results are compared to Mie calculations and good agreement is observed (typical error is within 10 %). Consequently, it can be assumed that multiple scattering effects are negligible and that the single scattering model is valid for a description of the OCT signal. From the data in Fig. 21.2a and the measured OCT magnitude at the interface, p_{NA} is determined using (21.6). Measurements of p_{NA} for all diameters are used to calculate the average heterodyne intensity back-coupling efficiency $Q = 0.26 \pm 0.04$, which is used to compare p_{NA} to Mie calculations in Fig. 21.2b. The experimental points match the calculated values reasonably well and the oscillations in p_{NA} due to the particle diameter dependent lobe structure of the backscattering efficiency are clearly observable.

The phase function in the backscattering direction p_{NA} can be used to estimate the average size of the scatterers and, consequently, g. To determine the average diameter, the crossing point of the horizontal line through the experimental p_{NA} and

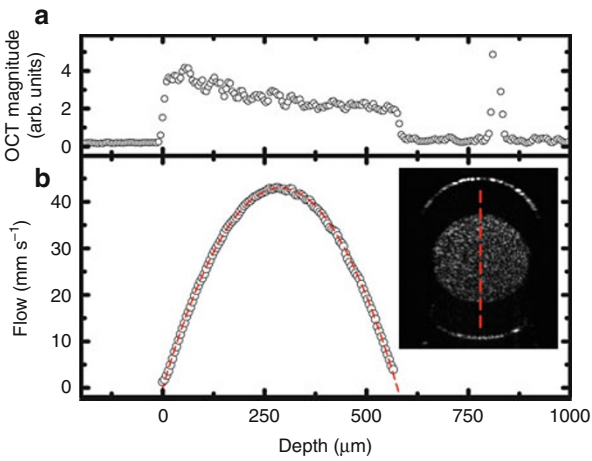

Fig. 21.3 (**a**) OCT signal and (**b**) Doppler OCT flow measurement of 0.5 vol% Intralipid solution under flow. The flow profile is measured in a cylindrical flow channel (see *inset*), the *vertical line* indicates the location of the flow measurement

the calculated p_{NA} curve for varying scatterer size has to be found. The obtained crossing point specifies the average particle diameter (Fig. 21.2b). Finally, the average particle diameter corresponds to a scattering anisotropy g (Fig. 21.2c). To demonstrate our method on non-calibrated samples we apply it to Intralipid, which is a polydisperse suspension of scatterers. Following the same procedure as for polystyrene microspheres, p_{NA} of Intralipid is determined. For low particle concentration, p_{NA} is independent of the concentration of scatterers and the p_{NA} values for all measured Intralipid concentrations (1.30×10^{-4}, 1.26×10^{-4} and 1.11×10^{-4} for 0.63, 1.25 and 2.5 wt% Intralipid, respectively) are averaged. The resulting value, $p_{NA} = (1.22 \pm 0.21) \times 10^{-4}$, is plotted in Fig. 21.2b. Note that although the refractive indices of polystyrene spheres and Intralipid droplets are different, this has negligible influence on the calculated p_{NA}. From Fig. 21.2b, the crossing point of the line of the calculated p_{NA} of polystyrene microspheres and the measured p_{NA} of Intralipid corresponds to a particle diameter of 438 ± 21 nm. Consequently, from Fig. 21.2c where we calculate g for varying particle diameter, this particle diameter corresponds to the scattering anisotropy $g = 0.35 \pm 0.03$. This value agrees very well with previously reported measurements of g for Intralipid at 1,300 nm $g = 0.32 \pm 0.07$ [13].

Doppler OCT experiments are conducted on a home-built spectral-domain (SD) OCT system operating at a center wavelength $\lambda_c = 1{,}300$ nm wavelength [14]. Doppler OCT measurements are performed by calculating the incremental phase change per A-line [15]. For low scattering media quantitative flow measurements can be performed using Doppler OCT. Figure 21.3 shows a Doppler OCT flow measurement on a 0.5 vol% Intralipid solution flowing through a glass capillary with 0.55 mm inner and 0.98 mm outer diameter. After calibration of the Doppler angle θ, quantitative flow measurements can be performed. The parabolic flow profile, predicted by the Navier–Stokes equations, is accurately measured using Doppler OCT.

21.4 Multiple and Dependent Scattering Effects in Doppler OCT Measurements of High Scattering Media

For low scattering media, the single scattering model is a good description of the Doppler OCT signal. At high particle concentrations and/or high scattering cross sections the scattering coefficient becomes high and multiple scattering is much stronger. Due to the nonzero collection *NA* and coherence length, multiple scattered light cannot be sufficiently rejected from the Doppler OCT signal, thereby affecting the measured Doppler OCT signal. As a result, the single scattering approximation is no longer valid and a quantitative analysis of the Doppler OCT signals is much more difficult.

Multiple scattering can lead to non-single-exponential decay, thereby making a quantitative determination of the scattering coefficient more difficult [16, 17]. Moreover, since in OCT the path length of the detected light is mapped one on one to a geometrical location in the sample, multiple scattering can also affect depth ranging and it can lead to spatial resolution loss [18]. For Doppler OCT flow measurements, it has been shown theoretically [19], with Monte Carlo (MC) simulations [20], and experimentally [21] that multiple scattering can increase or decrease the Doppler frequency for light penetrating deep into highly scattering media. Consequently, for a quantitative analysis of Doppler OCT data, e.g., to correctly determine flow and/or shear rate parameters [22], the effect of multiple scattering has to be taken into account.

In addition to multiple scattering, the scattering coefficient is also influenced by coherent light scattering effects, i.e., due to close packing of particles the coherent addition of light can lead to a reduction in the scattering coefficient. This effect is called dependent scattering; a dependence of the scattering strength on the separation between the particles. In this case, the scattering coefficient μ_s does not follow the linear relation $\mu_s = C\sigma_s$, but instead the Mie scattering cross section σ_s depends in a complex way on particle concentration C and therefore the relation $\mu_s = C\sigma_s(C)$ holds. As already shown in other light scattering experiments [23, 24], dependent scattering leads to a reduction in the scattering coefficient and thus can lead to a decrease of the OCT signal attenuation. In addition, the single scattering approximation of the scattering coefficient does not hold anymore and the scattering coefficient, in general, cannot be described as the sum of the contributions from the single scatterers. In this case, the scattering cross section becomes concentration dependent and coherent addition of waves scattered from different particles has to be taken into account.

To study multiple and dependent scattering effects, we perform Doppler OCT measurements of Intralipid and diluted blood solutions under flow with the SD-OCT system. For both samples the scattering strength varies with particle concentration. However, blood has a much higher scattering coefficient and scattering anisotropy than Intralipid. We will observe how these two effects influence multiple and dependent scattering.

As a scattering medium we use Intralipid. For Intralipid, we use dilutions of a single batch of 20 wt% Intralipid (Fresenius-Kabi) with distilled water. The

Intralipid (particle) volume concentration is calculated from the dilution of the batch solution by assuming that only the soybean oil and the egg-phospholipid are in the solid state, with the rest of the constituents (glycerol and water) in solution [25]. For blood, fresh porcine blood is drawn and anticoagulated before use. It is washed, centrifuged at 3,500 rpm, and the supernatant is replaced with phosphate buffered saline. Solutions with varying hematocrit (HCT) are made from the initial solution by adding phosphate buffered saline to the blood. For every solution a sample is taken right after the Doppler OCT measurement and analyzed with an XE-5000 automated hematology system to determine the mean cell volume (MCV) and HCT. Flow is generated by a precision syringe pump (Perfusor fm, B. Braun AG) that pumps the Intralipid solution at a flow of 50 or 100 mL/h through a 500 μm thickness glass flow cuvette with rectangular cross section.

Similar to the measurements with the time-domain OCT system, the SD-OCT signal magnitude is corrected for the signal background, confocal point spread function, and in addition, the spectral-domain depth detection sensitivity. Optical path length is converted to physical depth by dividing with an effective refractive index based on the relative concentrations of water ($n_{water} = 1.32$ [10]) and/or Intralipid ($n = 1.46$, soybean oil) and hemoglobin ($n_{Hb} = 1.40$, extrapolated from [26]). The Doppler frequencies are converted to flow using (21.7), the estimated refractive index, and the measured Doppler angle θ.

The OCT signal attenuation coefficient is determined by a 2-parameter single exponential fit (attenuation rate μ_{OCT} and amplitude) over a range in the cuvette where the signal shows a single exponential decay. Since the OCT signal at any depth z (path length) in the sample is attenuated by absorption according to $\exp(-\mu_a z)$, the fitted OCT attenuation coefficient is corrected for absorption by subtraction of the water and/or HCT dependent μ_a from μ_{OCT}. In this way, the OCT attenuation coefficient due to scattering only is obtained, which we call $\mu_{OCT,s}$.

Figure 21.4a and b show Doppler OCT measurements for 23 vol% Intralipid and (c) and (d) for HCT = 15 % blood. These concentrations are the highest concentrations we measured for Intralipid and blood. For Intralipid, the OCT signal attenuation is well described by a single exponential fit over the whole depth range of the cuvette, described by $\mu_{OCT,s} = 4.9\ \text{mm}^{-1}$. At this scattering coefficient the Doppler flow profile is not a parabola, as would be expected, but is severely distorted. The flow profile maximum is shifted from the center of the cuvette toward smaller depths and a large offset is observed at the bottom boundary of the cuvette. For blood, the OCT signal in the first 150 μm increases, thereafter it decreases with a single exponential decay, as described by $\mu_{OCT,s} = 4.9\ \text{mm}^{-1}$. The Doppler OCT flow profile for blood is distorted and shows, similar to Intralipid, a large offset at the bottom boundary of the flow profile.

The fits to the OCT signal decay in depth result in an estimation of $\mu_{OCT,s}$ for both Intralipid and blood as a function of concentration and is shown in Fig. 21.5. For both samples $\mu_{OCT,s}$ increases nonlinearly with increasing concentration. For Intralipid, $\mu_{OCT,s}$ is relatively close to μ_s as reported in literature [12, 13]. For similar volume concentrations $\mu_{OCT,s}$ for blood is close to that for Intralipid.

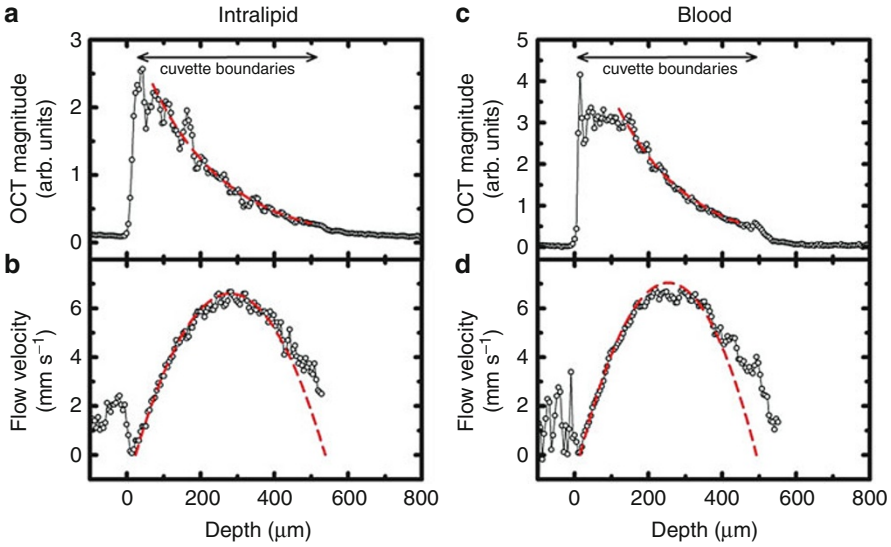

Fig. 21.4 (**a**) OCT and (**b**) Doppler OCT measurement for 23 vol% Intralipid and (**c**) OCT and (**d**) Doppler OCT for HCT = 15 % blood. Measured data is shown with *open circles*. Single exponential fits to the measured OCT signal are shown with *dashed line* in (**a**) and (**c**). Parabolic flow profile fits to the Doppler OCT signal are shown with a *dashed line* in (**b**) and (**d**)

However, we expect it to be much larger, since the scattering coefficient μ_s for blood is known to be much higher [27] than for Intralipid [12, 13].

21.5 Monte Carlo Simulations of Light Tissue Interaction in Scattering Media

Monte Carlo (MC) simulations are a powerful tool for simulating signals for a variety of experimental arrangements. Monte Carlo simulations of light tissue interaction have been widely used in OCT and Doppler OCT [18, 20]. Monte Carlo simulations of light tissue interaction are based on calculating the trajectories of a large numbers of photons randomly propagating in a scattering medium. Optical properties of the medium such as absorption coefficient, scattering coefficient, and scattering anisotropy determine the length and the shape path of individual photon trajectories. We use a traditional MC algorithm for simulation of light propagation in multilayered media described in Ref. [28], which is modified for simulation of OCT and Doppler OCT signals by accounting for the coherence gating and the geometry of the sample arm (shown in Fig. 21.6). Details of the Monte Carlo algorithm for OCT signal simulation can be found in [20]. To improve the calculation performance, a parallel message-passing-interface-based MC code was implemented on a computer cluster system based on Intel Xeon 3 GHz processors. For the simulation of a single OCT A-line scan, the trajectories of 10^{11} photons

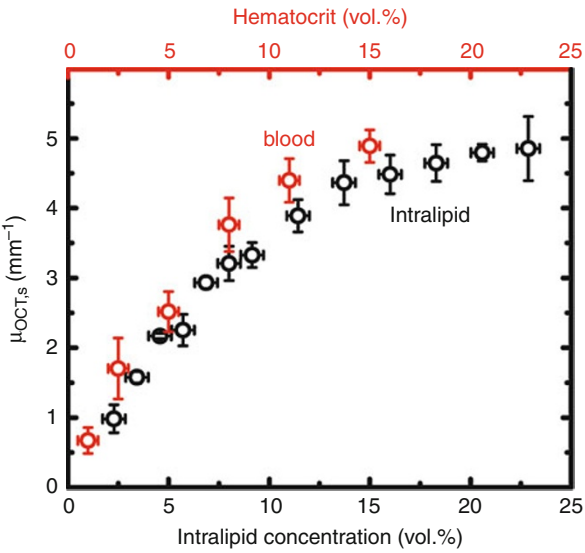

Fig. 21.5 Scattering coefficient $\mu_{OCT,s}$ measured with OCT for varying Intralipid concentration and blood HCT

were generated and analyzed. The incoming photons are modeled in the form of a pencil beam. Photons are considered to be coherent if their single pass optical path length is within half a coherence length of their maximum penetration depth. The outgoing photons are detected using a finite size detector located at the focal distance from the medium under study. We performed MC simulations for the SD-OCT system geometry and media describing Intralipid and blood. The sample arm geometry of this setup is shown in Fig. 21.6.

21.6 Monte Carlo Simulations of the Doppler OCT Signal

21.6.1 Monte Carlo Simulations of Doppler OCT Signals from Intralipid

To determine the role of multiple and dependent scattering on the OCT and Doppler OCT signal, we performed MC simulations using the developed MC code. First, we focus on Intralipid solutions, which have intermediate scattering coefficient and low scattering anisotropy. Figure 21.7 shows the simulated OCT signal as a function of depth calculated for the measured $\mu_{OCT,s}$ for three Intralipid concentrations (in Fig. 21.5). These simulations are performed using a Henyey-Greenstein function with $g = 0.33$ as a valid approximation of scattering phase function of Intralipid [13]. As can be seen from the figure, the simulated OCT signal decay is close to the expected scattering coefficient $\mu_{OCT,s}$, but for all Intralipid concentrations the slope of the single exponential part of the simulated OCT attenuation, indicated on the right hand side of the graph, is slightly lower ($\sim$13 %) than the input μ_s.

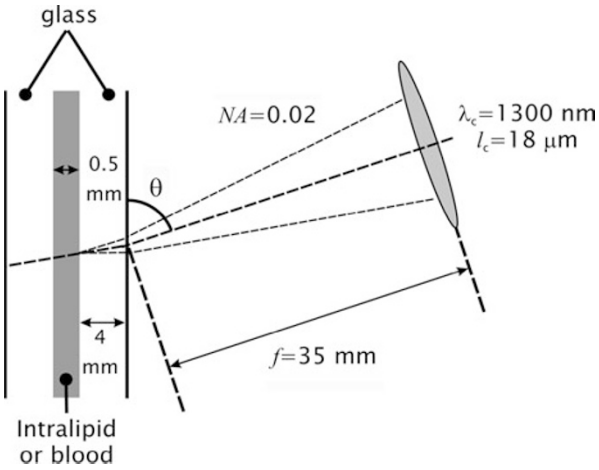

Fig. 21.6 Schematics of the sample arm configuration with focusing lens and flow cuvette. MC simulations are based on the geometry and experimental parameters: l_c is the coherence length of the source, f is the focal length of the sample arm lens, λ_c is the OCT center wavelength, NA is the numerical aperture of the lens, and θ is the Doppler angle

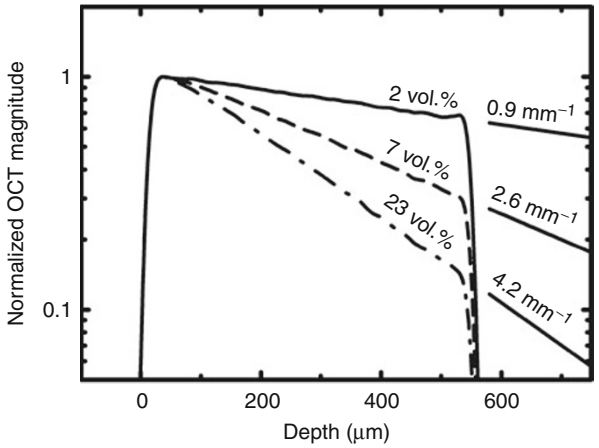

Fig. 21.7 Monte Carlo simulations of the OCT signal attenuation in depth for varying Intralipid concentration. The simulations are performed with $\mu_s = 1$, 2.9, and 4.9 mm^{-1}, for 2, 7, and 23 vol% Intralipid, respectively. Indicated on the *right* are the effective OCT attenuation coefficients $\mu_{OCT,s}$ obtained for these simulations

This phenomenon is clarified by an analysis of the contribution of multiple scattered photons, as is shown in Fig. 21.8.

Focusing on the highest Intralipid concentration, as shown in Fig. 21.8, the OCT signal from the single (back) scattered photons has an attenuation of μ_s, as expected. However, due to the finite collection numerical aperture and coherence length, multiple scattered photons are also detected. For depths larger than 200 μm the number of multiple scattered photons (scattered more than one time) exceeds the number of single scattered photons and since multiple scattered photons are found to have a lower attenuation rate with depth, their addition to the OCT signal from the single backscattered photons leads to a decrease of the attenuation coefficient from μ_s to $\mu_{OCT,s}$. Therefore, the OCT signal attenuation becomes slightly non-single exponential as it changes from mainly single backscattering

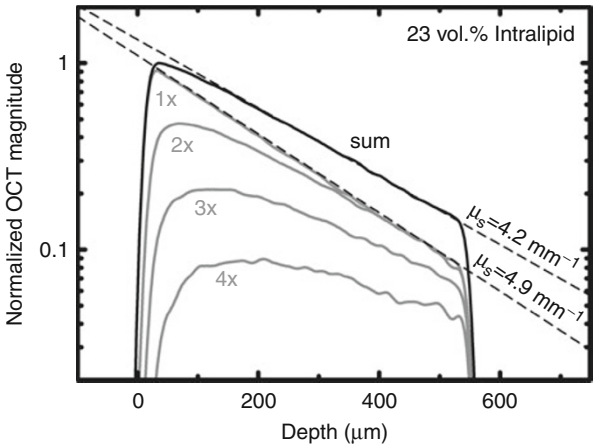

Fig. 21.8 Monte Carlo simulation of the OCT signal attenuation for 23 vol% Intralipid. The simulated OCT signal is decomposed into the contribution of the number of scattering events per photon (indicated). For single backscattering the attenuation is equal to the input μ_s. Multiple scattering adds signal to the OCT amplitude thereby decreasing the OCT attenuation coefficient from $\mu_s = 4.9\ \text{mm}^{-1}$ to $\mu_{OCT,s} = 4.2\ \text{mm}^{-1}$ (∼13 %)

(depth $<$ 200 μm) to mainly multiple scattered (depth $>$ 200 μm). From the MC simulations, we derive that we consistently underestimate the single scattering coefficient μ_s by ∼13 % if we compare the MC simulations to the measured OCT signal attenuation slope.

Next, we perform MC simulations of the Doppler OCT signal for flowing Intralipid. Figure 21.9 shows the simulated OCT Doppler signal using a normalized input flow for three different Intralipid concentrations. It demonstrates that for increasing Intralipid concentration the flow maximum shifts to a larger depth (+5 % relative to the center) and that the Doppler frequency at the rear border of the cuvette increases (+29 % of the peak flow), both are observed in our measurements (see Fig. 21.4b). Also, the peak flow decreases. This effect is difficult to observe in our measurements due to the flow variations of the syringe pump, dependence of the Doppler frequency on the refractive index of the Intralipid, and incidence angle variations due to the refractive index of the Intralipid. As expected, for single scattered photons the simulated Doppler flow profile is equal to the input parabolic flow profile (not shown).

21.6.2 Doppler OCT Signals for Varying Anisotropy Factor

In comparison with the single scattering description of the OCT signal, multiple scattering decreases the slope of the OCT signal in depth and affects the Doppler OCT flow profile at large depths. In general, these multiple scattering effects increase with increasing scattering coefficient. However, the effect of the scattering

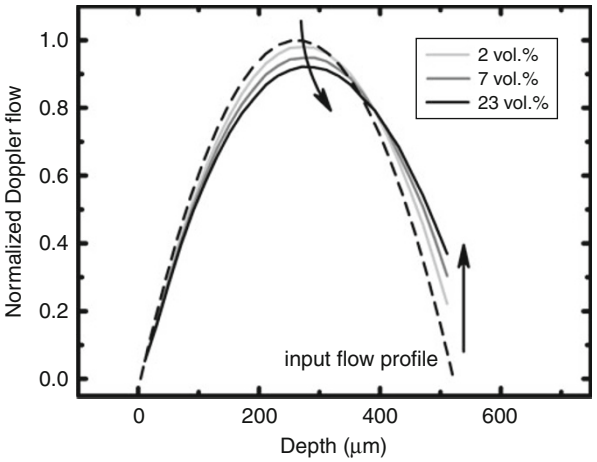

Fig. 21.9 Monte Carlo simulation of the Doppler OCT signal for varying Intralipid concentration. The *dashed line* indicates the input flow profile. The effect of increasing amounts of multiple scattering on the Doppler OCT signal is indicated by *arrows*

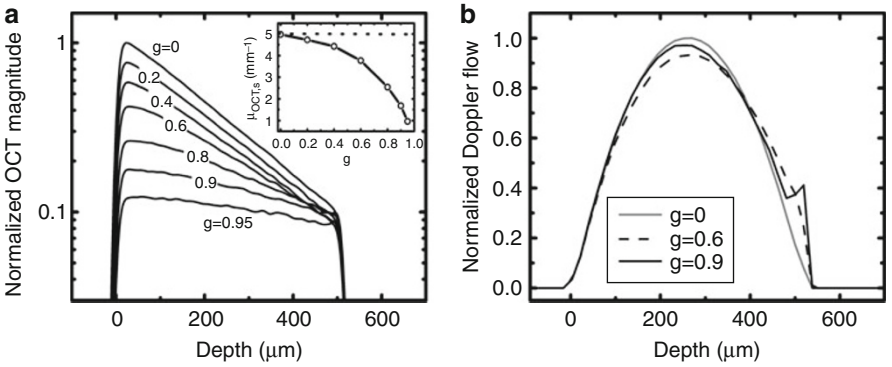

Fig. 21.10 (**a**) MC simulations of the OCT signal for different anisotropy factor g (values are indicated on the graph). The inset shows $\mu_{OCT,s}$ derived from the slope of the OCT signal for varying g-factor. (**b**) Normalized Doppler OCT flow profiles at selected g (indicated)

anisotropy g is more complicated, especially on the Doppler OCT flow profile. Figure 21.10 shows MC simulations using a constant $\mu_s = 5\ \text{mm}^{-1}$ and varying g (using a Henyey-Greenstein phase function). The simulations are performed for our experimental geometry. The absorption of the scattering medium is considered to be negligible small.

Figure 21.10a shows that the slope of the OCT signal decreases with increasing g due to increasing amounts of multiple scattered photons in the OCT signal. For $g = 0$, the slope of the OCT signal attenuation is close to that described by the single scattering model, which means that for this scattering anisotropy multiple scattered photons are effectively filtered out from the beam. For high scattering anisotropies (e.g., $g = 0.95$) many of the multiple scattered photons stay in the beam, thus

contributing to the OCT signal and decreasing its slope. This is further indicated in the inset where $\mu_{OCT,s}$ is estimated from the single exponential part of the decay and plotted against g. Figure 21.10b shows MC simulations for the Doppler OCT flow profiles at three different scattering anisotropies. For $g = 0$, the input flow profile is accurately reproduced because the Doppler OCT signal is formed mostly by single scattered photons. For $g = 0.6$ the flow profile is significantly distorted, and finally for $g = 0.9$, the flow profile again is slightly distorted, however, for this g the contribution of multiple scattered photons is significant. This effect can be explained by the interplay between the Doppler shift per scattering event and the average number of scattering events that a detected photon experiences. For very low g, the Doppler shift per scattering event is very large, however, these photons are very rapidly scattered sideways out of beam and do not contribute to the OCT signal. On the other hand, for very high g, photons are scattered mainly in the forward direction. These photons stay in the beam and contribute to the OCT signal, however, they have a very low Doppler shift per scattering event (strictly forward scattered photons have zero scattering angle and do not gain any Doppler shift). Therefore, the effect of multiple scattering on the measured Doppler OCT flow profile is largest at intermediate g, i.e., $g = 0.6$ where a significant fraction of the detected light is multiple scattered and these multiple scattered photons also experience a significant Doppler shift per scattering event. Forward scattering, which occurs at high g, also leads to the appearance of a small peak at the backside interface of the Doppler flow profile (Fig. 21.10b) even though the specularly reflected beam does not hit the detector (the capillary is tilted relative to the probe beam). This peak is formed by multiple (forward) scattered photons that are not present in the case when only single scattering is dominant.

21.6.3 Monte Carlo Simulations of Doppler OCT Signals from Blood

For high scattering media, such as blood, the effect of multiple scattering is expected to be much stronger than for Intralipid. For the OCT attenuation, this results in an underestimation of the scattering coefficient and a nonlinear increase of the scattering coefficient with HCT [17]. These effects are attributed to multiple scattering and concentration-dependent scattering, respectively. Here we use Monte Carlo (MC) simulations to model the Doppler OCT signal for flowing blood. It is well known that the Henyey-Greenstein function is not a good approximation for the red blood cell (RBC) phase function [29]. In addition, the experimentally obtained $\mu_{OCT,s}$ of blood is inadequately low to expect a good result of MC simulation using this parameter as input scattering coefficient. Therefore, the scattering cross section of an RBC is estimated using the discrete dipole approximation (DDA), calculated with the ADDA code [30]. The calculations are performed for $\lambda_c = 1{,}300$ nm using the RBC's dimensions (determined from the measured MCV as input parameter. The RBCs are modeled by oblate spheroid particles, this shape being the simplest nonspherical approximation for the RBC. For the refractive index contrast ratio we choose $|m| = 1.05$ [26]. The refractive index of the medium is estimated at $n_{med} = 1.33$. The ratio of the short over the long

axis lengths of the oblate spheroid is estimated to be 0.25 using Ref. [31]. As output of the DDA calculations, we obtain Mueller matrices for all scattering angles. For oblate spheroids, these Mueller matrices are calculated for two extreme orientations (short axis in the direction of the beam and short axis perpendicular to the beam). The M_{11} Mueller matrix elements (isotropic polarization scattering) are integrated over all scattering angles to obtain the scattering cross section and g. The scattering cross sections σ_s are converted to μ_s using the concentration C derived from the measured HCT and MCV values and the relation $\mu_s = C\sigma_s$, no concentration-dependent scattering effects are accounted in this calculation. The average phase function $p(\theta)$ is calculated, using the phase functions $p_0(\theta)$ and $p_{90}(\theta)$ and the scattering coefficients $\mu_{s,0}$ and $\mu_{s,90}$ at the two extreme orientations, according to [32] $p(\theta) = (\mu_{s,0}p_0(\theta) + \mu_{s,90}p_{90}(\theta))/(\mu_{s,0} + \mu_{s,90})$. The results of the calculations are shown in Fig. 21.11.

As expected, the calculated scattering coefficients for blood are significantly higher than the measured OCT scattering attenuation coefficient $\mu_{OCT,s}$. For very low HCT the difference between the calculated scattering coefficient and $\mu_{OCT,s}$ decreases. Figure 21.11a also shows the scattering coefficient determined by Roggan et al. [27] with the integrating sphere method at λ=1,300 nm and HCT = 5 % for human RBCs. Since the size of human RBCs is close to those of porcine RBCs [33] we expect that this value closely matches our DDA calculations, as is observed. Figure 21.11(b) shows the phase function integrated over the polar angle. The MC simulation uses the calculated RBC orientation-averaged phase function as input. The corresponding scattering anisotropy is $g = 0.98$.

Using the μ_s and phase function calculated with DDA as described above, we performed MC simulations for HCT = 8 %. This is the highest measured HCT below 10 % for which the linear relation between scattering coefficient and concentration holds (see Fig. 21.5 and Refs. [34, 35]) and avoids any concentration-dependent scattering effects.

Figure 21.12 shows the results of the MC simulations calculated with $\mu_s = 27\ \text{mm}^{-1}$ (HCT = 8 %, Fig. 21.11), $\mu_a = 0.37\ \text{mm}^{-1}$, and the orientation-averaged phase function. MC simulations are shown for the sum of all detected photons and for contributions according to the number of scattering events N a detected photon experienced. As can be seen, higher scattering orders are mainly deeper in the sample. The rise of the OCT signal in the first 100 μm is due to the buildup of higher scattering order signals. At the backside of the cuvette, most of photons have experienced more than 20 scattering events. The decay as a function of depth indicates much lower attenuation of the OCT signal compared to the single scattering model, i.e., $\mu_{OCT,s} = 3.8\ \text{mm}^{-1}$ versus $\mu_s = 27\ \text{mm}^{-1}$. Remarkably, $\mu_{OCT,s}$ estimated from the MC simulated OCT signal corresponds very well to the experimentally measured value (see Fig. 21.5). In Fig. 21.12b one can see that the Doppler OCT flow profile clearly deviates, albeit by a small amount, from a parabola, especially at the back end of the cuvette due to the multiple scattered photons contribution. Such a small deviation at a relatively high number of scattering events can be only explained by the high g of blood, which results in a very low Doppler shift per scattering event.

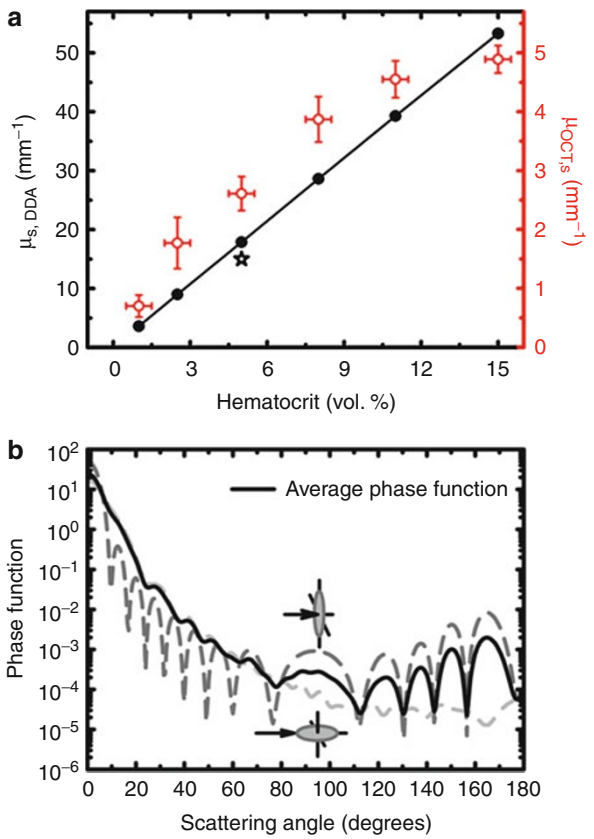

Fig. 21.11 (**a**) Orientation-averaged scattering coefficients calculated using DDA for oblate spheroids (shown with *black* color) and measured scattering coefficient $\mu_{OCT,s}$ (*red* color). The value for human RBCs [27] is indicated with a *star*. (**b**) Calculated RBC scattering phase function as a function of azimuthal angle: RBC short axis perpendicular to beam (*dashed light gray*), short axis parallel to beam (*dashed dark gray*), and average (*solid black*)

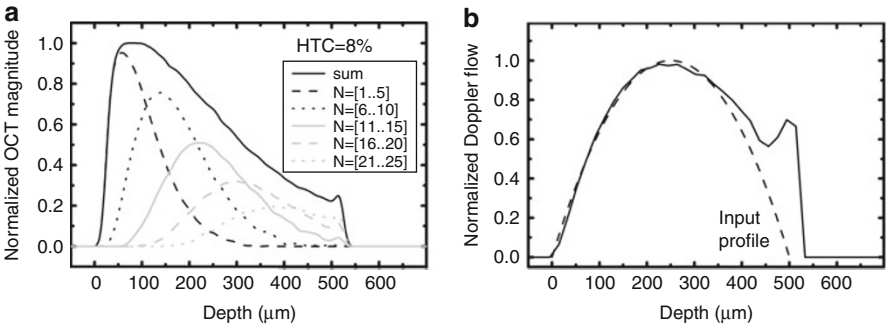

Fig. 21.12 (**a**) MC simulation of OCT signal from the porcine blood with HCT = 8 % for the sum over all photons (*black solid line*), and for different scattering orders N (see legend). (**b**) MC simulation of Doppler OCT signal (*black solid line*), and the input flow profile (*dashed line*)

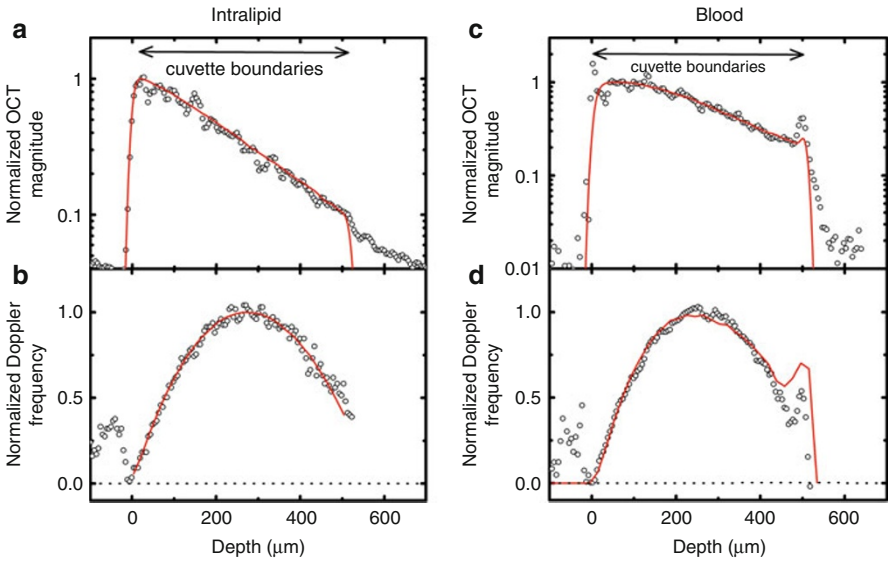

Fig. 21.13 (**a**) and (**b**) show the comparison of the measured OCT and Doppler OCT signals (*open dots*) with the results of MC simulation (*solid line*) (OCT amplitude signal and flow velocity profile) for 23 vol% Intralipid and (**c**) and (**d**) for HCT = 8 % blood

21.7 Comparison of Monte Carlo Simulations and Doppler OCT Measurements

To estimate the scattering coefficient of Intralipid at 23 vol% for which the experimental data and the MC simulation show good agreement, we performed a series of calculations for varying scattering coefficient. Good agreement is observed using $\mu_s = 5.6\ \text{mm}^{-1}$ as input parameter (see Fig. 21.13a). The input μ_s is 15 % higher than the scattering coefficient estimated from the OCT slope with the single scattering model ($\mu_{OCT,s} = 4.9\ \text{mm}^{-1}$). A relatively good single-exponential fit is also achieved for lower Intralipid concentrations (not shown). From a comparison of our OCT measurements and MC simulations, we conclude that for all Intralipid concentrations the scattering coefficient μ_s is approximately 15 % higher than the measured OCT signal attenuation rate due to multiple scattering effects. The MC simulation of Doppler OCT flow profile is compared to the experimental data and shown in Fig. 21.13b. Good agreement can be observed between the MC simulation and the measurements. Especially notable is that the offset of the flow at the deepest cuvette wall increases with Intralipid concentration in accordance with the measurements.

For blood with HCT = 8 % a good agreement in experimental and simulated OCT signal slopes was obtained with $\mu_s = 27\ \text{mm}^{-1}$. This value is also predicted by the DDA calculation using the simplified RBC model. The comparison of experimental and simulated data is shown in Fig. 21.13c. The increasing OCT signal at the

first glass/blood interface and the slope of the OCT signal as well as the small peak at the second blood/glass interface are well reproduced by the MC simulation. In Fig. 21.13d it can be observed that the MC simulation of the Doppler OCT flow profile matches the measured flow profile and is close to the single scattering model parabolic flow profile. The increase of the Doppler frequency at the second blood/glass interface is reproduced by the MC simulations albeit that the distortion of the MC simulated flow profile is larger than measured. For Doppler OCT measurements with HCT smaller than 8 %, similar agreement between Doppler OCT measurements and MC simulations is observed with the deviation between the single scattering model and measurements being smaller (not shown).

From our consistent agreement between the simulations and the measurements for both OCT signal attenuation and Doppler OCT data supports the interpretation of our data. Multiple scattering influences flow parameters measured with Doppler OCT such as peak flow, peak flow location, flow volume, and shear rate. To accurately quantify these parameters from Doppler OCT measurements in highly scattering media, multiple scattering effects have to be taken into account.

21.8 Conclusion

In this chapter, we have compared the Doppler OCT signals for low and high scattering media. We have shown that the single scattering model is an appropriate description for low scattering media. For low scattering media, parameters such as the scattering cross section, scattering anisotropy, and Doppler flow profile can be directly determined from the Doppler OCT signal.

For high scattering media, the single scattering model does not describe the OCT signal very well. Usually, the slope of the OCT signal is much lower than the scattering coefficient of the medium and the Doppler OCT flow profile is distorted. Both effects are caused by multiple scattered light that contributes to the OCT signal. The difference between the single scattering model description and the measured Doppler OCT signal depends on parameters of the sample under study (e.g., anisotropy factor) and parameters of the OCT setup (e.g., coherence length). We have shown that the scattering anisotropy is of paramount importance in the quantification of multiple scattering effects. For a medium with low scattering anisotropy (e.g., Intralipid, with $g = 0.32$ at 1,300 nm) the difference between the real scattering coefficient and the scattering coefficient estimated from the slope of the OCT signal is quite small. For the medium with a high scattering anisotropy (e.g., blood, with $g = 0.98$ at 1,300 nm) the scattering coefficient is much higher than predicted from the slope of the OCT signal using the single scattering description. Doppler OCT flow profiles are most strongly distorted at intermediate $g \sim 0.6$.

Acknowledgments A. V. Bykov acknowledges Finnish Funding Agency for Technology and Innovation (Tekes), FiDiPro project, No. 1027 21 2010. J. Kalkman is supported by the IOP Photonic Devices program managed by the Technology Foundation STW and Agentschap NL. The authors thank D. J. Faber, V. M. Kodach, T. G. van Leeuwen, J. van Marle, and G. J. Streekstra.

References

1. F.J. van der Meer, D.J. Faber, D.M. Baraznji Sassoon, M.C. Aalders, G. Pasterkamp, T.G. van Leeuwen, Localized measurement of optical attenuation coefficients of atherosclerotic plaque constituents by quantitative optical coherence tomography. IEEE Trans. Med. Imaging. **24**, 1369–1376 (2005)
2. Z. Chen, T.E. Milner, S. Srinivas, X. Wang, A. Malekafzali, M.J.C. van Gemert, J.S. Nelson, Noninvasive imaging of in vivo blood flow velocity using optical Doppler tomography. Opt. Lett. **22**, 1119–1121 (1997)
3. J.F. de Boer, T.E. Milner, M.J.C. van Gemert, J.S. Nelson, Two-dimensional birefringence imaging in biological tissue by polarization-sensitive optical coherence tomography. Opt. Lett. **22**, 934–936 (1997)
4. D. Huang, E.A. Swanson, C.P. Lin, J.S. Schuman, W.G. Stinson, W. Chang, M.R. Hee, T. Flotte, K. Gregory, C.A. Puliafito, J.G. Fujimoto, Optical coherence tomography. Science **254**, 1178–1181 (1991)
5. J.W. Goodman, *Statistical Optics* (Wiley, New York, 1985)
6. T.G. van Leeuwen, D.J. Faber, M.C. Aalders, Measurement of the axial point spread function in scattering media using single-mode fiber-based optical coherence tomography. IEEE J. Sel. Top. Quant. Electron. **9**, 227–233 (2003)
7. J.M. Schmitt, A. Knüttel, R.F. Bonner, Measurement of optical properties of biological tissues by low-coherence reflectometry. Appl. Opt. **32**, 6032–6042 (1993)
8. C. Akcay, P. Parrein, J.P. Rolland, Estimation of longitudinal resolution in optical coherence imaging. Appl. Opt. **41**, 5256–5262 (2002)
9. V.M. Kodach, J. Kalkman, D.J. Faber, T.G. van Leeuwen, Quantitative comparison of the OCT imaging depth at 1300 nm and 1600 nm. Biomed. Opt. Express **1**, 176–185 (2010)
10. M. Daimon, A. Masumura, Measurement of the refractive index of distilled water from the near-infrared region to the ultraviolet region. Appl. Opt. **46**, 3811–3820 (2007)
11. A. Unterhuber, B. Povazay, B. Hermann, H. Sattmann, W. Drexler, V. Yakovlev, G. Tempea, C. Schubert, E.M. Anger, P.K. Ahnelt, M. Stur, J.E. Morgan, A. Cowey, G. Jung, T. Le, A. Stingl, Compact, low-cost Ti:Al_2O_3 laser for in vivo ultrahigh-resolution optical coherence tomography. Opt. Lett. **28**, 905–907 (2003)
12. H.J. van Staveren, C.J.M. Moes, J. van Marle, S.A. Prahl, M.J.C. van Gemert, Light scattering in Intralipid-10 % in the wavelength range of 400–1100 nm. Appl. Opt. **30**, 4507–4514 (1991)
13. C. Chen, J.Q. Lu, H. Ding, K.M. Jacobs, Y. Du, X. Hu, A primary method for determination of optical parameters of turbid samples and application to intralipid between 550 and 1630 nm. Opt. Express **14**, 7420–7435 (2006)
14. J. Kalkman, A.V. Bykov, D.J. Faber, T.G. van Leeuwen, Multiple and dependent scattering effects in Doppler optical coherence tomography. Opt. Express **18**, 3883–3892 (2010)
15. L. Wang, Y. Wang, S. Guo, J. Zhang, M. Bachman, G.P. Li, Z. Chen, Frequency domain phase-resolved optical Doppler and Doppler variance tomography. Opt. Commun. **242**(4–6), 345–350 (2004)
16. L. Thrane, H.T. Yura, P.E. Andersen, Analysis of optical coherence tomography systems based on the extended Huygens–Fresnel principle. J. Opt. Soc. Am. A **17**(3), 484–490 (2000)
17. D.J. Faber, T.G. van Leeuwen, Are quantitative attenuation measurements of blood by optical coherence tomography feasible? Opt. Lett. **34**(9), 1435–1437 (2009)
18. R.K. Wang, Signal degradation by multiple scattering in optical coherence tomography of dense tissue: a Monte Carlo study towards optical clearing of biotissues. Phys. Med. Biol. **47**(13), 2281–2299 (2002)
19. H.T. Yura, L. Thrane, P.E. Andersen, Analysis of multiple scattering effects in optical Doppler tomography. Proc. SPIE **5861**, 5861B (2005)
20. A.V. Bykov, M.Y. Kirillin, A.V. Priezzhev, Monte Carlo simulation of an optical coherence Doppler tomography signal: the effect of the concentration of particles in a flow on the reconstructed velocity profile. Quant. Electron. **35**(2), 135–139 (2005)

21. J. Moger, S.J. Matcher, C.P. Winlove, A. Shore, The effect of multiple scattering on velocity profiles measured using Doppler OCT. J. Appl. Phys. D. **38**(15), 2597–2605 (2005)
22. T.G. van Leeuwen, M.D. Kulkarni, S. Yazdanfar, A.M. Rollins, J.A. Izatt, High-flow-velocity and shear-rate imaging by use of color Doppler optical coherence tomography. Opt. Lett. **24**(22), 1584–1586 (1999)
23. G. Göbel, J. Kuhn, J. Fricke, Dependent scattering effects in latex-sphere suspensions and scattering powders. Waves Rand. Comp. Med. **5**, 413–426 (1995)
24. G. Zaccanti, S. Del Bianco, F. Martelli, Measurements of optical properties of high-density media. Appl. Opt. **42**, 4023–4030 (2003)
25. R. Michels, F. Foschum, A. Kienle, Optical properties of fat emulsions. Opt. Express **16**, 5907–5925 (2008)
26. M. Friebel, M. Meinke, Determination of the complex refractive index of highly concentrated hemoglobin solutions using transmittance and reflectance measurements. J. Biomed. Opt. **10**, 064019 (2005)
27. A. Roggan, M. Friebel, K. Dörschel, A. Hahn, G. Müller, Optical properties of circulating human blood in the wavelength range 400–2500 nm. J. Biomed. Opt. **4**, 36–46 (1999)
28. L. Wang, S.L. Jacques, L. Zheng, MCML – Monte Carlo modeling of light transport in multi-layered tissues. Comput. Methods Programs Biomed. **47**(2), 131–146 (1995)
29. A.N. Yaroslavsky, I.V. Yaroslavsky, T. Goldbach, H.-J. Schwarzmaier, Influence of the scattering phase function approximation on the optical properties of blood determined from the integrating sphere measurements. J. Biomed. Opt. **4**(1), 47–53 (1999)
30. M.A. Yurkin, V.P. Maltsev, A.G. Hoekstra, The discrete dipole approximation for simulation of light scattering by particles much larger than the wavelength. J. Quant. Spectrosc. Radiat. Transfer **106**, 546–557 (2007)
31. A.V. Cardoso, A.O. Camargos, Geometrical aspects during formation of compact aggregates of red blood cells. Mater. Res. **5**, 263–268 (2002)
32. V.M. Kodach, D.J. Faber, J. van Marle, T.G. van Leeuwen, J. Kalkman, Determination of the scattering anisotropy with optical coherence tomography. Opt. Express **19**, 6131–6140 (2011)
33. J.E. Smith, N. Mohandas, S.B. Shohet, Variability in erythrocyte deformability among various mammals. Am. J. Physiol. **236**, 725–730 (1979)
34. J.M. Steinke, A.P. Shepherd, Role of light scattering in whole blood oximetry. IEEE Trans. Biomed. Eng. **33**, 294–301 (1986)
35. M. Meinke, G. Müller, J. Helfmann, M. Friebel, Empirical model functions to calculate hematocrit-dependent optical properties of human blood. Appl. Opt. **46**, 1742–1753 (2007)